



Title	Diagnostics for Near-Surface Wind Response to the Gulf Stream in a Regional Atmospheric Model
Author(s)	Takatama, Kohei; Minobe, Shoshiro; Inatsu, Masaru; Small, R. Justin
Citation	Journal of Climate, 28(1), 238-255 <a href="https://doi.org/10.1175/JCLI-D-13-00668.1">https://doi.org/10.1175/JCLI-D-13-00668.1</a>
Issue Date	2015-01
Doc URL	<a href="http://hdl.handle.net/2115/59445">http://hdl.handle.net/2115/59445</a>
Rights	© Copyright 2015 American Meteorological Society (AMS). Permission to use figures, tables, and brief excerpts from this work in scientific and educational works is hereby granted provided that the source is acknowledged. Any use of material in this work that is determined to be "fair use" under Section 107 of the U.S. Copyright Act September 2010 Page 2 or that satisfies the conditions specified in Section 108 of the U.S. Copyright Act (17 USC § 108, as revised by P.L. 94-553) does not require the AMS' s permission. Republication, systematic reproduction, posting in electronic form, such as on a web site or in a searchable database, or other uses of this material, except as exempted by the above statement, requires written permission or a license from the AMS. Additional details are provided in the AMS Copyright Policy, available on the AMS Web site located at ( <a href="http://www.ametsoc.org/">http://www.ametsoc.org/</a> ) or from the AMS at 617-227-2425 or <a href="mailto:copyrights@ametsoc.org">copyrights@ametsoc.org</a> .
Type	article
File Information	jcli_28_p238-.pdf



[Instructions for use](#)



## Diagnosics for Near-Surface Wind Response to the Gulf Stream in a Regional Atmospheric Model\*

KOHEI TAKATAMA

*International Pacific Research Center, University of Hawai'i at Mānoa, Honolulu, Hawaii, and Graduate School of Science, Hokkaido University, Sapporo, Hokkaido, Japan*

SHOSHIRO MINOBE AND MASARU INATSU

*Graduate School of Science, Hokkaido University, Sapporo, Hokkaido, Japan*

R. JUSTIN SMALL

*Climate and Global Dynamics Division, National Center for Atmospheric Research, Boulder, Colorado*

(Manuscript received 31 October 2013, in final form 10 September 2014)

### ABSTRACT

The mechanisms acting on near-surface winds over the Gulf Stream are diagnosed using 5-yr outputs of a regional atmospheric model. The diagnostics for the surface-layer momentum vector, its curl, and its convergence are developed with a clear separation of pressure adjustment from downward momentum inputs from aloft in the surface-layer system. The results suggest that the downward momentum mixing mechanism plays a dominant role in contributing to the annual-mean climatological momentum curl, whereas the pressure adjustment mechanism plays a minor role. In contrast, the wind convergence is mainly due to the pressure adjustment mechanism. This can be explained by the orientation of background wind to the sea surface temperature front. The diagnostics also explain the relatively strong seasonal variation in surface-layer momentum convergence and the small seasonal variation in curl. Finally, the surface-layer response to other western boundary currents is examined using a reanalysis dataset.

### 1. Introduction

Recent high-resolution satellite observations have significantly advanced the understanding of how the ocean and atmosphere interact on monthly or longer time scales. These observations have revealed that the divergence and curl<sup>1</sup> of near-surface horizontal wind exhibit remarkable structures over large-scale sea surface temperature (SST)

fronts, where the SST significantly changes within several tens or hundreds of kilometers [see Xie (2004), Chelton et al. (2004), Small et al. (2008), and Chelton and Xie (2010) for reviews]. Using observations by the Quick Scatterometer (QuikSCAT) satellite launched in 1999 (Liu 2002), Liu et al. (2000) and Chelton et al. (2001) found surface wind divergence in response to the downwind component of the SST gradient and surface wind curl in response to the crosswind component of the SST gradient associated with tropical instability waves. Xie et al. (2002) reported a similar wind response in the midlatitudes to the Kuroshio in the East China Sea. Following these studies, the distinct response of near-surface wind to midlatitude SSTs has been widely observed over the western boundary currents, such as the Kuroshio in the south of Japan (Nonaka and Xie 2003), the Kuroshio Extension (Liu and Xie 2008; Tokinaga et al. 2009), the Gulf Stream (Chelton et al. 2004; Xie 2004; Minobe et al. 2008), the Agulhas Return Current

<sup>1</sup> Throughout the paper, “curl” is taken to represent the vertical component only.

\* International Pacific Research Center Contribution Number IPRC-1083.

Corresponding author address: K. Takatama, International Pacific Research Center, University of Hawai'i at Mānoa, POST Bldg., 1680 East-West Road, Honolulu, HI 96822.  
E-mail: takatama@hawaii.edu

(O'Neill et al. 2003, 2005; Liu et al. 2007), and the Brazil–Malvinas confluence (Tokinaga et al. 2005). Furthermore, the significant effect of sharp SST fronts is not limited to the marine atmospheric boundary layer (MABL): The induced near-surface wind curl is thought to play an important role in oceanic Ekman pumping (Chelton et al. 2007), and the convergence is considered responsible for precipitation enhancement, deep ascent in the midtroposphere, and frequent occurrences of high clouds (Minobe et al. 2008; Iizuka 2010; Miyama et al. 2012; Hand et al. 2014).

There has been much debate on the mechanisms of the near-surface wind response to SST fronts, which has now come down to two major hypotheses. One mechanism is conventionally called the vertical mixing mechanism. Here, the near-surface atmosphere is destabilized over warmer SSTs, resulting in intensified downward momentum transport from aloft, which acts to accelerate the surface wind (Sweet et al. 1981; Wallace et al. 1989; Hayes et al. 1989). This mechanism explains the commonly observed feature of near-surface wind speed generally being large on the warm flank of an SST front (e.g., Hayes et al. 1989; Chelton et al. 2001; Xie et al. 2002; O'Neill et al. 2003; Small et al. 2008). When background wind blows parallel to an SST front, this mechanism yields horizontal curls of near-surface winds. On the other hand, when background wind blows over a warm-to-cold SST gradient across a front, the mechanism yields horizontal convergence of near-surface winds (Spall 2007). Hereinafter, we use the term “downward momentum mixing (DMM) mechanism” to refer to downward momentum transport from aloft that should be externally given in the surface-layer system.

The second hypothesized mechanism is the pressure adjustment (PA) mechanism, originally suggested by Lindzen and Nigam (1987). In the present paper, we define the PA mechanism as follows. Sharp SST contrasts across a front strongly modify air temperature in the MABL, making sea level pressure (SLP) concave on the warm side and convex on the cold side. The low (high) pressure anomalies produce cyclonic (anticyclonic) circulation and induce surface wind convergence over warm SSTs and divergence over cold SSTs. The effect may be manifested in the Laplacian of SLP (Minobe et al. 2008; Bryan et al. 2010; Putrasahan et al. 2013) and can also be extracted by a spatial high-pass filter that masks meridional background SLP gradients in the midlatitudes (Tokinaga et al. 2009; Minobe et al. 2010; Tanimoto et al. 2011). When advection of temperature in the MABL is important, the SLP pattern is shifted downwind side relative to the SST pattern, as seen in the atmospheric response to tropical instability waves (Small et al. 2003). This temperature advection effect is, however, not important over western boundary

currents, because an SST Laplacian (Minobe et al. 2008) or a satellite-derived Laplacian of thickness between the 1000- and 850-hPa isobaric levels as a substitute for SLP modified by MABL (Shimada and Minobe 2011) does not exhibit substantial shift to the wind convergence.

Reviewing the debate on the mechanism noted above, the previous studies basically examined an empirical estimation. Chelton et al. (2001) showed that the near-surface wind curl is linearly related to the crosswind component of the SST gradient, and the divergence of near-surface wind is linearly related to the downwind component of the SST gradient. This is the same as in the case of the DMM mechanism that often acts in the tropics as well as in western boundary current regions (e.g., Chelton et al. 2001; O'Neill et al. 2003; Chelton et al. 2004; Maloney and Chelton 2006). In another study, Minobe et al. (2008) proposed that convergence of near-surface wind due to the PA mechanism is proportional to the Laplacian of SLPs. This relationship also holds true in major western boundary current regions, both in observations (Minobe et al. 2008; Shimada and Minobe 2011) and in recent high-resolution numerical modeling (Kuwano-Yoshida et al. 2010; Bryan et al. 2010). These results indicate that these two mechanisms work simultaneously in nature, and previous studies tried to determine contributions of these mechanisms using momentum budget analysis.

Conventional diagnostics have been performed by using the momentum equation at a given height (Wai and Stage 1989; Small et al. 2003; Song et al. 2006; Skyllingstad et al. 2007; Spall 2007), as given by

$$\frac{\partial \mathbf{u}}{\partial t} + (\mathbf{u} \cdot \nabla) \mathbf{u} + f \mathbf{k} \times \mathbf{u} = -\frac{1}{\rho} \nabla p + \frac{1}{\rho} \frac{\partial \boldsymbol{\tau}}{\partial z}, \quad (1)$$

where  $\mathbf{u}$  is the horizontal wind vector,  $f$  the Coriolis parameter,  $\mathbf{k}$  the vertical unit vector,  $p$  the atmospheric pressure,  $\rho$  the atmospheric density, and  $\boldsymbol{\tau}$  the wind shear stress. In Eq. (1), horizontal diffusion terms are ignored. Takatama et al. (2012) pointed out that the diagnostics using Eq. (1) do not completely separate the two mechanisms, because the turbulent stress shear includes the downward momentum input from aloft as well as the damping due to the surface stress; the latter is actually an internal product in the surface-layer system in which both DMM and PA mechanisms possibly work. Moreover, Takatama et al. (2012) proposed that the two mechanisms can be separated by taking the vertical average of Eq. (1) over the surface layer, assuming that the surface stress is proportional to the vertically averaged horizontal wind momentum. Their resultant equation of the time-mean vertically averaged momentum divergence successfully separated the term for the pressure from the term for the downward momentum inputs from aloft.

The purpose of the present paper is to provide a comprehensive explanation of the diagnostics and analysis of the near-surface wind in response to western boundary currents. Based on the diagnostics by Takatama et al. (2012) that are limited to near-surface wind convergence, we extend these diagnostics to include near-surface wind and wind curl. Our diagnostics are applied to spatially high-resolution and temporally dense data on wind, pressure, and turbulence in order to analyze a long-term model experiment focusing on the Gulf Stream region. Here we treat the annual mean and the seasonal cycle of the atmospheric response in this region. Furthermore, we attempt to apply our diagnostics to other western boundary currents, even where the dataset is limited and we therefore cannot fully diagnose the response, and we discuss the generality of the diagnostics in regard to air–sea interactions in the midlatitudes.

The remainder of the present paper is organized as follows. The new diagnostic method and numerical experimental design are described in section 2. Relative contributions of the two mechanisms to annual-mean state are investigated in section 3. Seasonal variations in the response are described in section 4. An application of the diagnostics to other SST frontal regions using high-resolution reanalysis data is discussed, and the conclusions are presented in section 5.

## 2. Method

### a. Diagnostics

Taking the time average for Eq. (1) and then vertically averaging from the sea surface to the top of the surface layer  $Z$ , we obtain the time-mean surface-layer momentum equation as

$$-fV = -P_x + [\tau^x(Z) - \tau^x(0)]/Z + A^x \quad \text{and} \quad (2a)$$

$$+fU = -P_y + [\tau^y(Z) - \tau^y(0)]/Z + A^y, \quad (2b)$$

where  $x$  and  $y$  designate the zonal and meridional coordinates, respectively;  $U$  and  $V$  are the vertically averaged zonal and meridional momenta, respectively;  $P$  is the vertical average of air pressures;  $\tau^x(Z)$  and  $\tau^y(Z)$  are the downward momentum inputs from the top of the surface layer at the height  $Z$  by vertical diffusion and vertical advection;  $\tau^x(0)$  and  $\tau^y(0)$  are the surface wind stress vectors; and  $A^x$  and  $A^y$  are the horizontal advection component vectors. Here, the subscripts denote derivatives. Although the advection terms depend on  $(U, V)$ , we formally treat these terms as if they are forcing for simplicity. We show later that the contribution of the advection is much smaller than that of the pressure

gradient and the downward momentum transport, so the major results would not change if the advection terms were removed from Eq. (2).

A key point of our diagnostics is the discrimination between the momentum input down to the surface layer  $\tau(Z)$  and the surface wind stress  $\tau(0)$ . The former is externally given from the surface-layer system, and it is considered to be the forcing of the DMM mechanism. Although one might argue that the downward momentum input term can be affected by wind speed change at or above the top of the surface layer due to the PA mechanism, that term is still essentially controlled by the DMM mechanism; wind speed change across the Gulf Stream at the top of the surface layer is about 10%, much smaller than the change of momentum input of about 50% in our standard experiment described below. In contrast,  $\tau(0)$  is generated by not only the DMM mechanism but also the PA mechanism, because the surface stress is internally determined in the surface-layer system and would be generally given as a complicated function of wind velocity. Here, in order to divide the surface stress into the DMM and PA components, we simply assume that it is linearly proportional to  $U$  and  $V$  as follows:

$$\frac{\tau^x(0)}{Z} = \varepsilon U \quad \text{and} \quad \frac{\tau^y(0)}{Z} = \varepsilon V. \quad (3)$$

These equations describe the Rayleigh friction and are widely used for layer models (e.g., Lindzen and Nigam 1987). Here, the frictional parameter  $\varepsilon$  varies spatially but not temporally and is determined at each grid point. By comparing Eq. (3) with a bulk formula (Deardorff 1968), we see that  $\varepsilon$  depends on atmospheric instability via the drag coefficient, as well as on background wind speed. However, if we use spatially constant  $\varepsilon$  instead of the spatially varying one, our results are essentially unchanged, as shown below. The above assumption is consistent with O’Neill (2012), who showed that small-scale wind stress perturbations are linearly proportional to wind speed perturbations with the relation modulated nonlinearly by background wind speeds.

Using Eq. (3) for the surface wind stress, Eq. (2) can be solved for the vertically averaged momentum  $U$  and  $V$ :

$$\begin{bmatrix} U \\ V \end{bmatrix} = \frac{1}{\varepsilon^2 + f^2} \begin{bmatrix} \varepsilon & f \\ -f & \varepsilon \end{bmatrix} \begin{bmatrix} -P_x + \tau^x(Z)/Z + A^x \\ -P_y + \tau^y(Z)/Z + A^y \end{bmatrix}. \quad (4)$$

The vertically averaged momentum is now expressed by a sum of the terms for pressure gradient, downward momentum inputs, and horizontal momentum advection. As shown below, the pressure gradient (downward

momentum input) term does not necessarily include solely the PA (DMM) mechanism, but roughly represents the

corresponding mechanism. From Eq. (4), the curl of vertically averaged momentum can be written as

$$V_x - U_y = \left[ \frac{f}{\varepsilon^2 + f^2} \nabla^2 P - M_1 P_y + M_2 P_x \right] + \left[ \frac{\varepsilon}{\varepsilon^2 + f^2} \frac{\nabla \times \boldsymbol{\tau}(Z)}{Z} - \frac{f}{\varepsilon^2 + f^2} \frac{\nabla \cdot \boldsymbol{\tau}(Z)}{Z} + M_1 \frac{\tau^y(Z)}{Z} - M_2 \frac{\tau^x(Z)}{Z} \right] + \left[ \frac{\varepsilon}{\varepsilon^2 + f^2} \nabla \times \mathbf{A} - \frac{f}{\varepsilon^2 + f^2} \nabla \cdot \mathbf{A} + M_1 A^y - M_2 A^x \right], \quad (5)$$

where  $M_1 = [\varepsilon/(\varepsilon^2 + f^2)]_x + [-f/(\varepsilon^2 + f^2)]_y$  and  $M_2 = [\varepsilon/(\varepsilon^2 + f^2)]_y + [f/(\varepsilon^2 + f^2)]_x$ . The curl of vertically averaged momentum is also divided into three groups of terms: the pressure terms (first set of brackets), the

downward momentum input terms (second set of brackets), and the horizontal advection terms (third set of brackets). Similarly, the convergence of vertically averaged momentum can be written as

$$-U_x - V_y = \left[ \frac{\varepsilon}{\varepsilon^2 + f^2} \nabla^2 P + M_1 P_x + M_2 P_y \right] + \left[ -\frac{\varepsilon}{\varepsilon^2 + f^2} \frac{\nabla \cdot \boldsymbol{\tau}(Z)}{Z} - \frac{f}{\varepsilon^2 + f^2} \frac{\nabla \times \boldsymbol{\tau}(Z)}{Z} - M_1 \frac{\tau^x(Z)}{Z} - M_2 \frac{\tau^y(Z)}{Z} \right] + \left[ -\frac{\varepsilon}{\varepsilon^2 + f^2} \nabla \cdot \mathbf{A} - \frac{f}{\varepsilon^2 + f^2} \nabla \times \mathbf{A} - M_1 A^x - M_2 A^y \right]. \quad (6)$$

On the right-hand side of Eq. (6), the terms in the first, second, and third set of brackets represent the terms for pressure, downward momentum inputs, and horizontal advection, respectively (Takatama et al. 2012).

Recall from the reviews cited in section 1 that the PA mechanism is manifested in the Laplacian of SLPs. Strictly speaking, this corresponds to only the first term in the first set of brackets in Eqs. (5) and (6). Terms containing  $M_1$  and  $M_2$  are mainly associated with spatial change of frictional parameter  $\varepsilon$  and are not regarded as describing the PA mechanism. As will be shown later, the PA mechanism term is much larger than the other pressure terms, consistent with Lindzen and Nigam (1987). If the  $M_1$  and  $M_2$  terms are dominant in Eqs. (5) and (6), the strong surface damping over warmer SSTs will reduce near-surface wind speeds (Businger and Shaw 1984). Similarly, the DMM mechanism corresponds to only the first term in the second set of brackets in Eqs. (5) and (6). The second term is also a function of the downward momentum transfer, but this is not the DMM mechanism originally proposed for the tropics (Wallace et al. 1989; Hayes et al. 1989), because it represents a Coriolis effect that emerges in only the midlatitudes (Tokinaga et al. 2005). The remaining terms containing  $M_1$  and  $M_2$  are associated with mainly spatial change of the frictional parameter and do not represent the DMM mechanism, either. As will be shown later, the DMM mechanism term is dominant among the terms for downward momentum inputs.

The height  $Z$  in Eq. (2) should be set to the top of the surface layer for near-surface diagnosis. Because the surface layer occupies approximately one-tenth of the

MABL and the annual-mean MABL height ranges between 700 and 1200 m, here we set the height  $Z$  to 100 m. Moreover, to separate frontal-scale atmospheric response from large-scale circulation, in particular the curl field, we used a spatial high-pass filter following previous studies (e.g., Chelton et al. 2004) retaining a wavelength shorter than  $30^\circ$  in longitude and latitude. Although the spatial high-pass filter is effective for masking large-scale background circulation, the filter does not affect the main results even for the curl field. All results shown below have been subjected to high-pass filtering, unless otherwise stated.

### b. Model and experiments

The regional atmospheric model used in this study is the International Pacific Research Center Regional Climate model (iRAM). The model includes dynamical processes based on hydrostatic formulation and physical parameterizations such as radiative transfer, shallow and deep convection, and turbulent mixing [see Wang et al. (2003) for details]. The model uses an  $E$ - $\varepsilon$  turbulent closure scheme for vertical diffusion and a modified Monin–Obukhov scheme for turbulent fluxes at the ocean surface.

We conducted two experiments: a standard experiment with a  $0.5^\circ \times 0.5^\circ$  horizontal grid and a high-resolution experiment with a  $0.25^\circ \times 0.25^\circ$  horizontal grid. For both the experiments, the vertical layers are 28 sigma layers. The model domain fully covers the western North Atlantic ( $5^\circ$ – $65^\circ$ N,  $100^\circ$ – $20^\circ$ W). We used the National Centers for Environmental Prediction (NCEP) Reanalysis-1 with a  $2.5^\circ$  grid at 6-hourly intervals (Kalnay et al. 1996) for the initial and lateral boundary conditions in both the

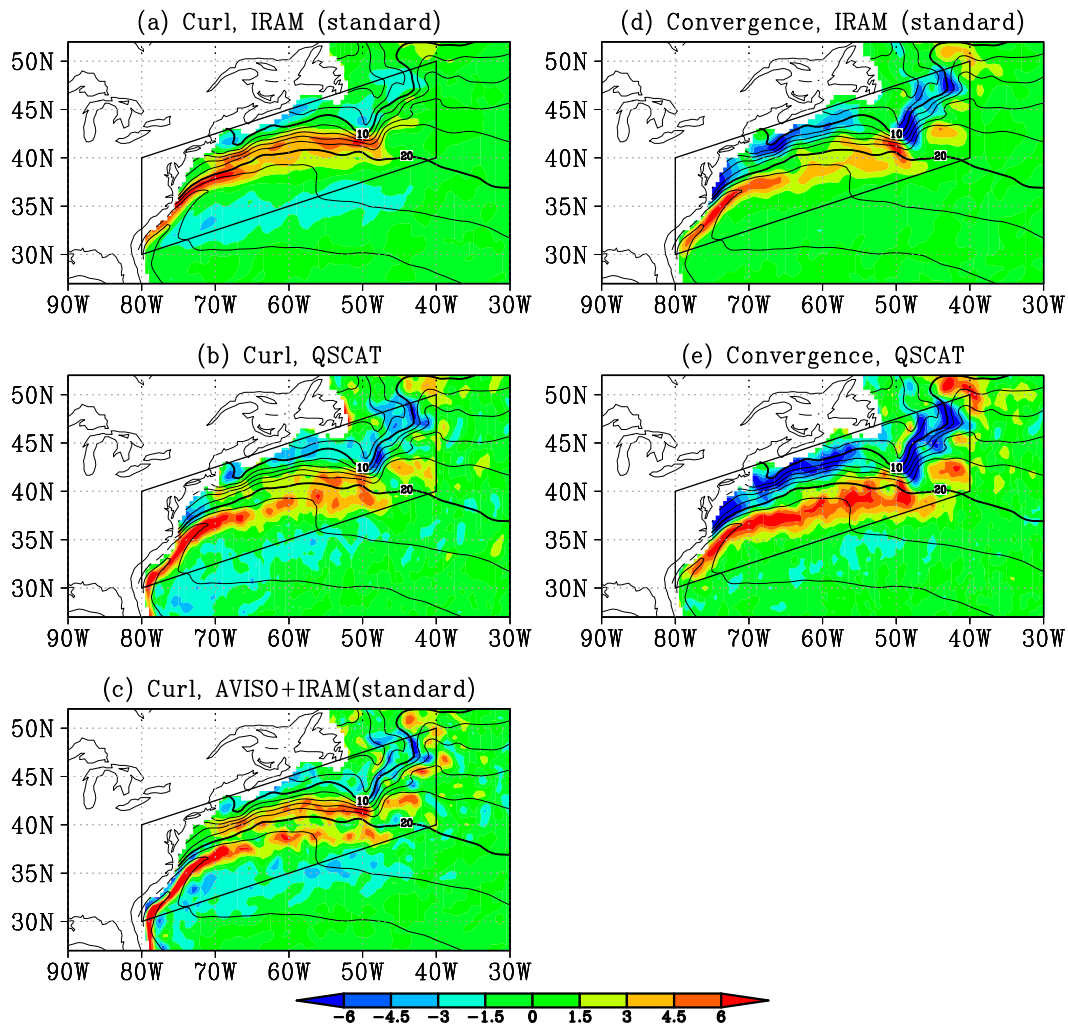


FIG. 1. (a)–(c) Annual-mean climatology of neutral 10-m wind curl (color,  $10^{-6} \text{ s}^{-1}$ ) obtained from (a) the standard experiment of iRAM's simulation, (b) satellite observation by QuikSCAT, and (c) the simulated wind curl in the standard experiment relative to ocean current provided by AVISO data. Contours show annual-mean climatology of nonfiltered SST; contour interval is  $2^{\circ}\text{C}$ . The parallelogram area is for statistics along the SST front. (d), (e) Annual-mean climatology of 10-m wind convergence (color,  $10^{-6} \text{ s}^{-1}$ ) obtained from (d) the standard experiment and (e) satellite observation by QuikSCAT. In the figures below, unless otherwise specified, figures show the results of the standard experiment, and contours indicate the SST.

experiments. NCEP Real-Time Global SST (RTGSST) with a  $0.5^{\circ} \times 0.5^{\circ}$  grid at daily intervals (Gemmill et al. 2007) was used as the surface boundary condition for the standard experiment and the National Oceanic and Atmospheric Administration (NOAA) optimum interpolation (OI) SST, with a  $0.25^{\circ} \times 0.25^{\circ}$  grid, including Advanced Very High Resolution Radiometer (AVHRR) and Advanced Microwave Scanning Radiometer for Earth Observing System (AMSR-E) at daily intervals (Reynolds et al. 2007), was used for the high-resolution experiment. The standard experiment was integrated for 5 yr from December 2001 to November 2006, and the high-resolution was integrated for 1 yr from December

2003 to November 2004 after a 1-month spinup. The integration period of standard experiment is one to two orders of magnitude longer than those used in previous diagnostic studies on the atmospheric response to SST fronts (e.g., Small et al. 2003; Song et al. 2006; O'Neill et al. 2010) to obtain a robust result of the stationary response.

The standard experiment successfully captured the major features of the surface wind response around the Gulf Stream. Consistent with observations (Chelton et al. 2004; Xie 2004), annual-mean climatology of 10-m wind in the model exhibits cyclonic circulation from the warm flank to the center of the SST front and anticyclonic circulation over the cold flank (Fig. 1a). Compared with the

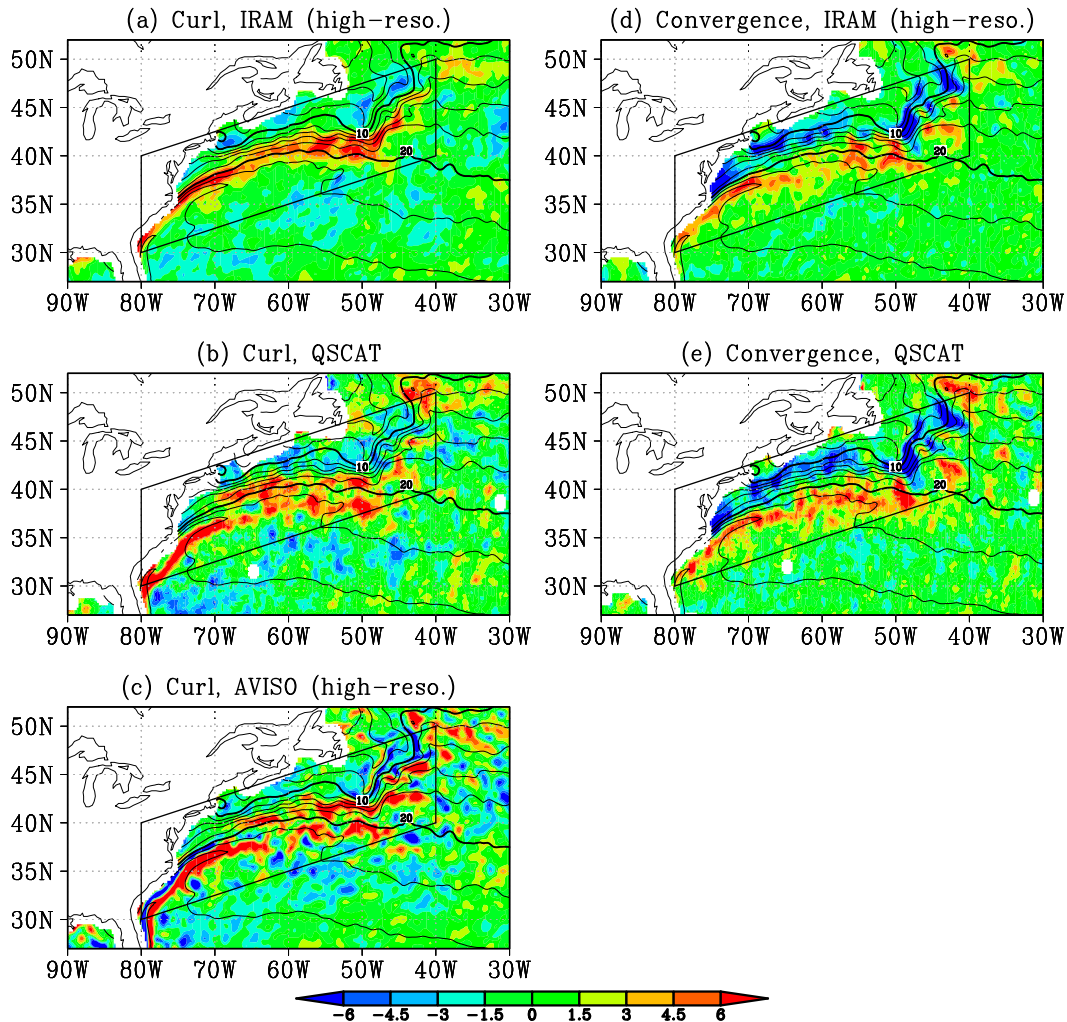


FIG. 2. As in Fig. 1, but the simulated fields are obtained from the high-resolution experiment. The statistics are calculated over 1 yr from December 2003 to November 2004.

QuikSCAT data on a  $0.5^\circ \times 0.5^\circ$  grid available from the Jet Propulsion Laboratory (Fig. 1b), the simulation underestimates the cyclonic curl south of the  $20^\circ\text{C}$  SST contour. This is mainly because the wind speed estimated from scatterometric data is affected by surface ocean current, as suggested by Chelton et al. (2004). When the surface wind is calculated as a relative speed to oceanic surface geostrophic current, provided from Archiving, Validation, and Interpretation of Satellite Oceanographic (AVISO) data on a  $0.5^\circ \times 0.5^\circ$  grid, the resultant curl well reproduces the spatial pattern of the satellite observation (Fig. 1c). On the other hand, near-surface wind converges (diverges) over the warm (cold) flank of the SST front (Fig. 1d), consistent with previous studies (Minobe et al. 2008, 2010). This is quite similar to the QuikSCAT observation (Fig. 1e).

The standard experiment somewhat underestimates the convergence compared with that obtained by QuikSCAT, and this problem is improved in the

high-resolution experiment (Fig. 2). The spatial standard deviation of the annual-mean convergence obtained from QuikSCAT over the parallelogram area shown in Figs. 1 and 2 is  $3.61 \times 10^{-6} \text{ s}^{-1}$  for a same period of the high-resolution experiment. This value increases from  $2.75 \times 10^{-6} \text{ s}^{-1}$  in the standard experiment to  $3.15 \times 10^{-6} \text{ s}^{-1}$  in the high-resolution experiment. However, the high-resolution integration exhibit higher variability in small-scale structures of the curl and convergence (Figs. 2a,d). This may be at least partly due to the short integration, because QuikSCAT results also shows more energetic small-scale variations for 1-yr average (Figs. 2b,e) than those for 5-yr average (Figs. 1b,e). This indicates that to assess representative mean state, 5-yr average may be better than 1-yr average. Therefore, we mainly use the results of the standard experiment in the rest of the paper, but we will mention results of the high-resolution experiment where they are appropriate.

In essence, the major conclusions in the present paper do not depend on the model resolutions.

### 3. Diagnostics of annual-mean state

#### a. Frictional parameter

Before performing the diagnostics, we first show the characteristics of the frictional parameter  $\varepsilon$ , which plays an important role in our method. This parameter is determined from annual-mean wind stress and vertically averaged momentum as

$$\varepsilon(x, y) = Z \sqrt{[\tau^x(0)]^2 + [\tau^y(0)]^2} / \sqrt{U^2 + V^2} \quad (7)$$

at each grid point.<sup>2</sup> Figure 3a shows a scatterplot of vertically averaged horizontal momentum and surface stress magnitude around the SST front (the parallelogram area of Fig. 1). Note that we exclude the region where the vertically averaged momentum is less than  $1 \text{ kg m s}^{-1}$  to obtain stable estimation of  $\varepsilon$  and exclude regions within two grid points from the coastline to avoid the effects of land. In the scatterplot, the parameter  $\varepsilon$  at each grid point corresponds to the slope of the line that connects a single dot with the origin. The frictional parameter can be classified into two groups: high  $\varepsilon$  over the regions where SSTs are higher than the surface-layer temperature by more than 2 K (red dots in Fig. 3a) and low  $\varepsilon$  elsewhere (blue dots). The regions of high and low  $\varepsilon$  correspond to the regions that are likely unstable or stable, respectively (Fig. 3b). Nevertheless, there is only a small spatial change in the parameter  $\varepsilon$ , whose  $\pm 1$  standard deviation range is  $1.79 \pm 0.20 \times 10^{-4} \text{ s}^{-1}$  over the parallelogram region, reflecting almost linear relation between the vertically averaged momentum and the surface stress (spatial correlation is 0.93). Therefore, if we use a constant  $\varepsilon$ , the diagnostic results are essentially unchanged. This is further supported by the fact that the terms, including  $M_1$  and  $M_2$  in Eqs. (5) and (6), are negligibly small.

Related to the well-defined frictional parameter around the Gulf Stream region (Fig. 3b), the simulation data sufficiently satisfy the diagnostics of Eqs. (4)–(6). As for Eq. (4), the simulated momentum on the left-hand side has a high spatial correlation with the diagnosed momentum on the right-hand side, with a correlation coefficient of 1.00 for zonal wind and 0.96 for meridional wind. Similarly, the simulated curl [left-hand side of Eq. (5)] is almost identical

<sup>2</sup> One can directly estimate the frictional parameter in Eq. (3) independently for zonal and meridional wind; however, these values are almost the same as those in Eq. (7).

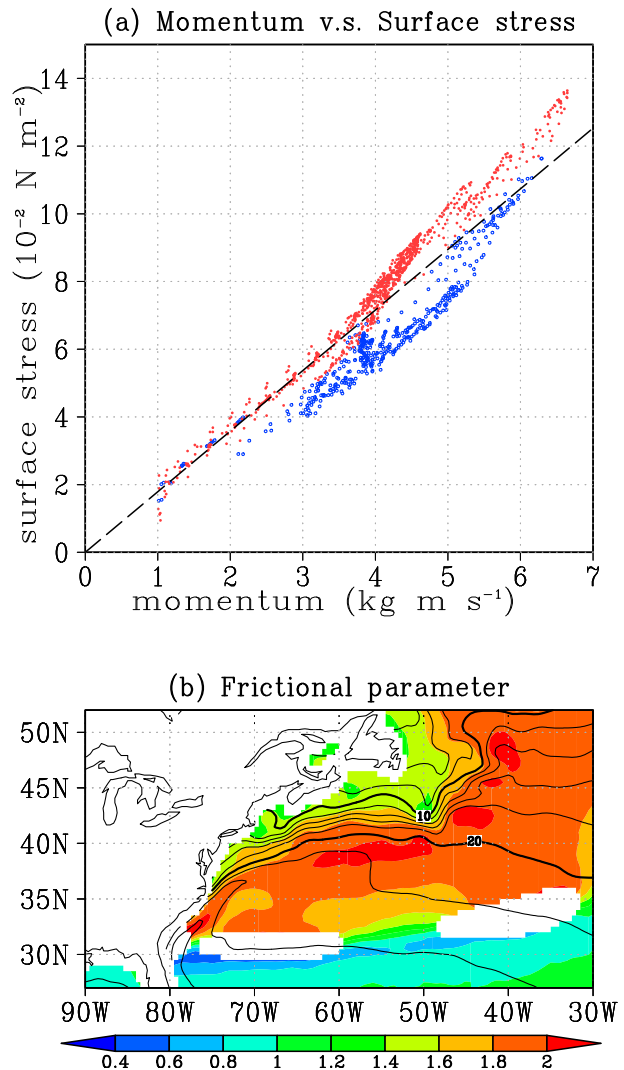


FIG. 3. (a) Scatterplot of annual-mean surface-layer momentum ( $\text{kg m s}^{-1}$ ) vs sea surface wind stress ( $10^{-2} \text{ N m}^{-2}$ ) in the parallelogram area shown in Fig. 1. Red dots indicate points where SST is  $>2 \text{ K}$  higher than surface-layer temperature, and blue dots indicate elsewhere. The slope of the line connecting the origin and each point corresponds to the value of the frictional parameter  $\varepsilon$  at each grid point. Dashed line denotes the area-averaged  $\varepsilon$  ( $1.79 \times 10^{-4} \text{ s}^{-1}$ ). See the text for the definition of  $\varepsilon$ . (b) Horizontal distribution of frictional parameter  $\varepsilon$  (color,  $10^{-4} \text{ s}^{-1}$ ). The region where the absolute momentum is less than  $1 \text{ kg m s}^{-1}$  is excluded from (a) and (b).

to the diagnosed curl [right-hand side of Eq. (5)]; their spatial correlation is 0.90 and the regression coefficient of the diagnostics onto the simulation is 1.08 (Figs. 4a,b). The diagnosed convergence is also highly correlated with the simulated convergence (Figs. 4c,d). It is worth noting that the diagnostic variables vertically averaged over the surface layer (Fig. 4) are quite similar to those based on neutral 10-m wind (Figs. 1a,d), indicating that

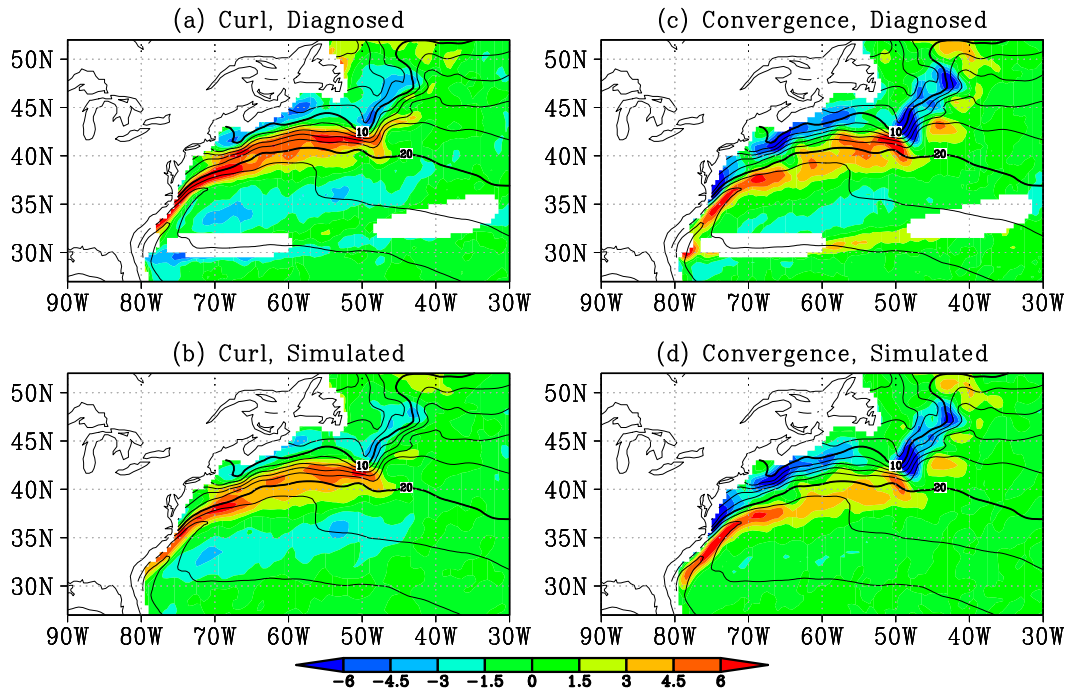


FIG. 4. (a) Diagnosed surface-layer wind curl [right-hand side of Eq. (5)] and (b) the simulated one [left-hand side of Eq. (5)] ( $10^{-6} \text{ kg s}^{-1}$ ). The region where the absolute momentum is less than  $1 \text{ kg m s}^{-1}$  is excluded from the diagnostics. (c) Diagnosed surface-layer wind convergence [right-hand side of Eq. (6)] and (d) simulated surface-layer wind convergence [left-hand side of Eq. (6)].

surface-layer momentum is representative of near-surface wind.

### b. Contribution of each mechanism

Figure 5 shows the division of the diagnosed momentum vector into three components consisting of the pressure terms, the downward momentum input terms, and the horizontal advection terms, respectively, based on Eq. (4). The pressure gradient generates wind anomalies in the across-front direction over steep SST gradients from cold SST regions to warm ones, with overall meridional wind anomalies in a wider area arising from the large-scale pressure gradient, whereas the downward momentum transport mainly contributes to a zonal momentum anomaly. Because  $\varepsilon$  is about twofold larger than  $f$ , as noted above, the geostrophy plays only a minor role in Eq. (4), and thus the wind momentum vectors in the left-hand side should be nearly parallel to the forcings in the right-hand side. Indeed, the wind anomaly due to the pressure gradient force blows into the warm flank of the front and out of the cold flank, consistent with the pressure pattern expected from the PA mechanism, as explained in section 1. The westerly wind anomaly due to the downward momentum transport occurs on the warm flank of the front in the direction of the background wind, and the easterly wind

anomaly occurs on the cold flank against the background wind. This is consistent with the DMM mechanism, since the relatively large (small) momentum from westerly aloft is brought to the surface layer over the warm (cold) or unstable (stable) region.

Figures 6a–c show the divided contributions to momentum curl from the three components corresponding to the three sets of brackets on the right-hand side of Eq. (5). The simulated curl (Fig. 4b) is dominated by the downward momentum input terms (Fig. 6b). This produces strong cyclonic curl just over the front and weak anticyclonic curl over the front's cold flank. The pressure terms (Fig. 6a) and the horizontal advection terms (Fig. 6c) are less than half of the downward momentum input terms. To evaluate their contribution to wind curl, we conduct a spatial regression analysis, in which we regress each term of Eq. (5) onto the simulated momentum curl: that is, the left-hand side of Eq. (5). Consistently, the regression coefficient for the downward momentum input terms is about 3 (5) times larger than that for the pressure (advection) terms. Furthermore, Table 1 shows the first term corresponding to the DMM (PA) mechanism is actually the largest among the downward momentum input (pressures) terms in the second (first) set of brackets in Eq. (5). These features found in the standard experiment are essentially

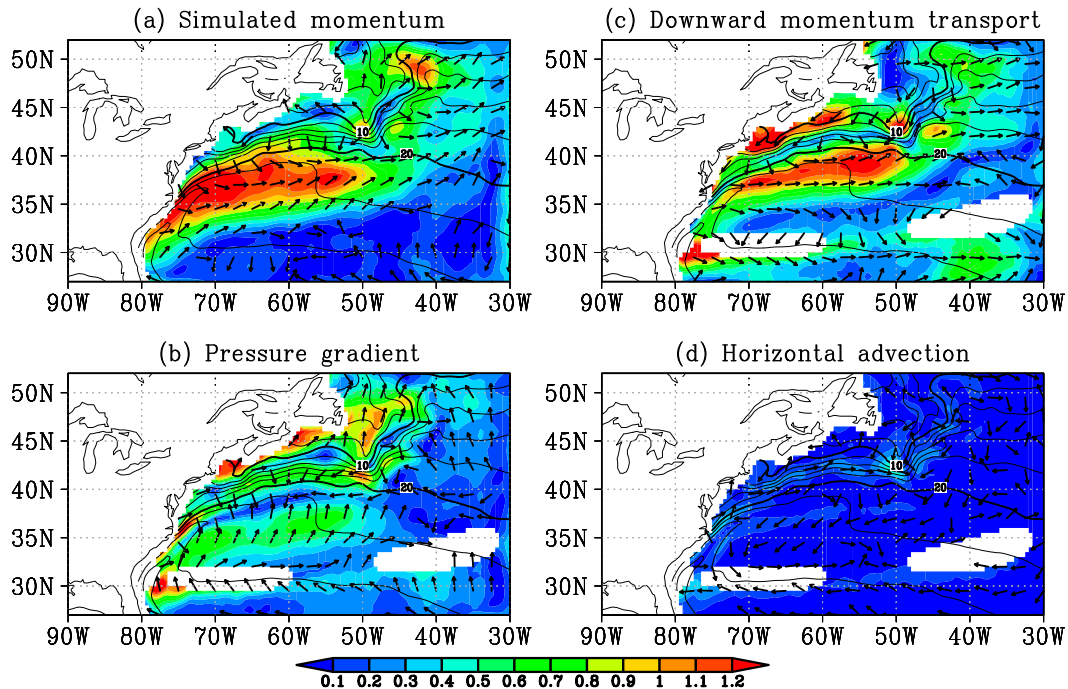


FIG. 5. (a) Simulated momentum vector and its diagnosed components resulting from (b) the pressure gradient, (c) downward momentum transport, and (d) horizontal advection. Vector length is normalized, and its magnitude is indicated by color ( $\text{kg m s}^{-1}$ ).

reproduced in the high-resolution experiment (Table 1). Therefore, the surface-layer wind curl is mostly explained by the DMM mechanism, but the PA mechanism cannot be ignored.

In contrast to the dominant contribution of the DMM mechanism to the momentum curl, the momentum convergence is mostly explained by the PA mechanism. The sum of pressure terms (Fig. 6d) dominantly contributes to the momentum convergence, accompanied by a much weaker contribution of the downward momentum input terms (Fig. 6e). The pressure terms contribute to the convergence on the warm side and the divergence on the cold side along the SST front. The downward momentum input terms, on the other hand, contribute to convergence (divergence) just to the west (east) of a sharp northward turn of the Gulf Stream near the Grand Banks. The contribution of horizontal advection is quite small (Fig. 6f). This diagnostic for surface wind convergence based on the spatially filtered data is consistent with that in Takatama et al. (2012) based on unfiltered data. Regression analysis confirms that the term for the PA mechanism is the largest among the pressure terms, and the regression coefficient for the PA mechanism is more than 4 times larger than that for the DMM mechanism (Table 1). The PA mechanism appears to be more dominant in the high-resolution experiment than in the standard experiment, and the

regression coefficient of the PA mechanism is now 10 times larger than the DMM mechanism. Consequently, the momentum convergence is mostly explained by the PA mechanism.

The spatial patterns of curl and convergence resulting from the pressure terms (Figs. 6a,d) are essentially determined by the Laplacian of vertically averaged pressure (Fig. 7a), which is the largest term among the pressure terms in Eqs. (5) and (6). The momentum curl and convergence due to the PA mechanism are given by  $f\nabla^2 P/(\varepsilon^2 + f^2)$  and  $\varepsilon\nabla^2 P/(\varepsilon^2 + f^2)$  in Eqs. (5) and (6), respectively, and thus the magnitude of difference between them is explained by the difference between the frictional parameter  $\varepsilon$  and the Coriolis parameter  $f$ . The typical value of  $\varepsilon$  is about twofold larger than  $f$ , and hence the PA mechanism contributes more strongly to momentum convergence than to momentum curl. Because pressure anomalies do not change much vertically within the lowest 100 m, the Laplacian of the surface-layer mean pressure is proportional to the SLP Laplacian (not shown). Hence, as Minobe et al. (2008) suggested, the SLP Laplacian is a good measure of near-surface wind convergence due to the PA mechanism. Likewise, it is apparent that the SLP Laplacian also represents curl due to the PA mechanism. The distinct pressure anomalies around the Gulf Stream are definitely caused by surface heat flux, because we find good correspondence among

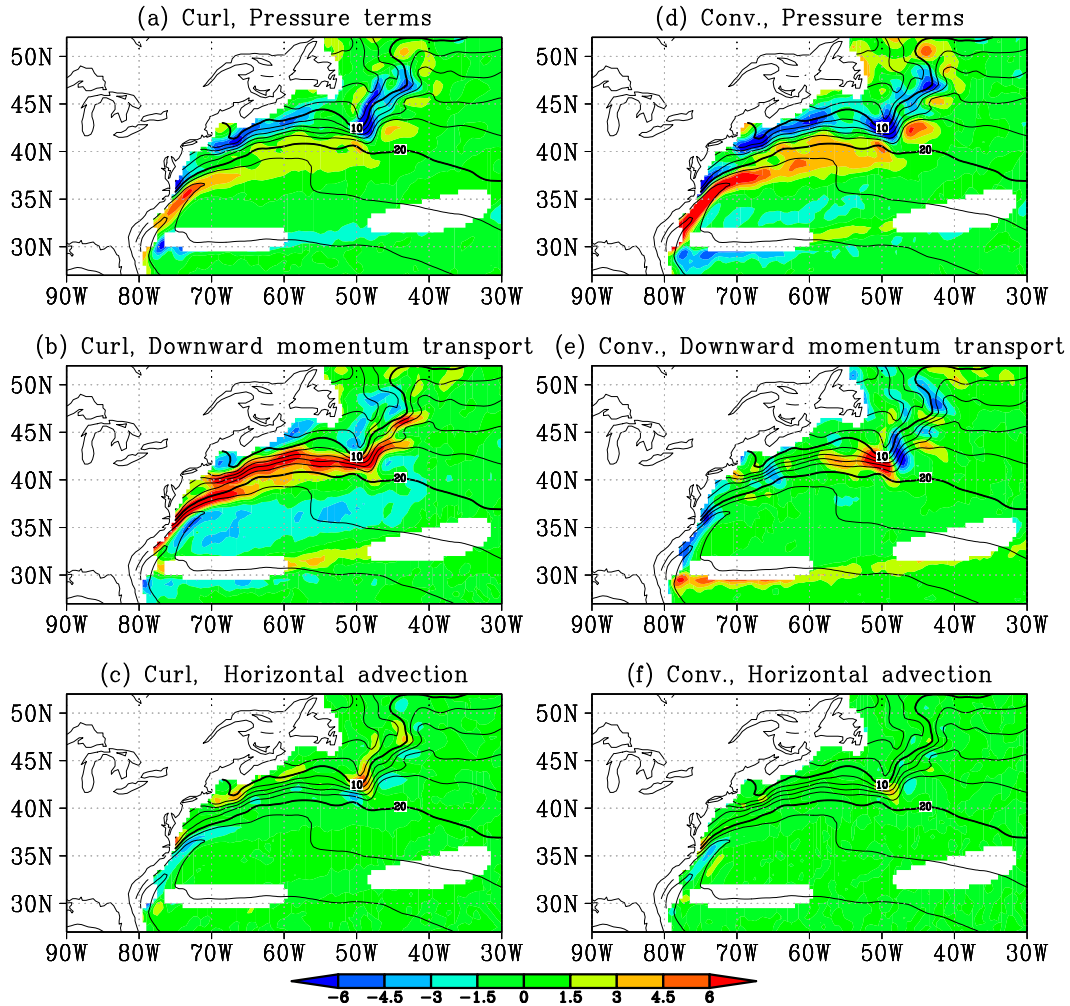


FIG. 6. Momentum curl (color,  $10^{-6} \text{ kg s}^{-1}$ ) resulting from the (a) pressure terms, (b) downward momentum input terms, and (c) horizontal advection terms in Eq. (5). Momentum convergence (color,  $10^{-6} \text{ kg s}^{-1}$ ) resulting from the (d) pressure terms, (e) downward momentum input terms, and (f) horizontal advection terms in Eq. (6).

the pressure Laplacian, sign-reversed temperature Laplacian (Fig. 7b), and sensible heat fluxes to the atmosphere (Fig. 7c), consistent with Brachet et al. (2012). Here we show the sensible heat flux, because this would be mainly responsible for heating of the MABL, but the pattern of the sensible plus latent heat flux is almost the same as that of the sensible heat flux. The flux difference across the SST front exceeds  $250$  ( $80$ )  $\text{W m}^{-2}$  for the latent plus sensible (sensible only) heat flux.

The DMM mechanism contributes to surface-layer momentum curl via the curl of the downward momentum input  $\nabla \times \tau(Z)$  and surface-layer momentum convergence via the divergence of the downward momentum input  $\nabla \cdot \tau(Z)$  [Eqs. (5) and (6)]. The curl of the momentum input (Fig. 8a) is highly correlated with the sign-reversed crosswind SST gradient  $-\mathbf{v}_{10} \times \nabla T$  (Fig. 8b). Here  $\mathbf{v}_{10}$  is the annual-mean climatology of

the 10-m wind vector, and  $T$  is the SST. Similarly, the convergence of the momentum input (Fig. 8c) is highly correlated with the sign-reversed downwind SST gradient  $-\mathbf{v}_{10} \cdot \nabla T$  (Fig. 8d). This is consistent with previous studies (e.g., Chelton et al. 2001). Here, we employ  $\mathbf{v}_{10}$  for background wind for a better comparison of the previous studies, but the results are essentially unchanged if 850-hPa winds are used for the background wind. Since the westerly blows approximately parallel to the SST front over a large portion of the Gulf Stream west of  $55^\circ\text{W}$ , the crosswind SST gradient is large there, leading to the enhanced curl of downward momentum transport. In contrast, the westerly blows approximately perpendicular to the front in the downstream region of the Gulf Stream (east of  $55^\circ\text{W}$ ), where the downwind SST gradient and thus the downward momentum convergence have large

TABLE 1. Spatial regression coefficients of diagnosed momentum curl and momentum convergence on the simulations. Pressure (downward momentum input) terms indicate the sum of all the terms in the first (second) bracket in the right-hand side of Eq. (5) for curl and Eq. (6) for convergence, while the terms on the PA and DMM mechanisms indicate the first term in the respective brackets.

	Standard experiment		High-resolution experiment	
	Curl	Convergence	Curl	Convergence
Pressure terms	0.36	0.91	0.37	1.01
Term on the PA mechanism	0.35	0.99	0.37	1.06
Downward momentum input terms	1.01	0.20	0.93	0.06
Term on the DMM mechanism	1.05	0.22	0.87	0.10
Horizontal advection terms	-0.21	-0.11	-0.16	-0.11

magnitudes and the relative contribution of the PA mechanism on the curl is large.

### c. Term balance with retention of surface stress

As described in section 2a, in our diagnostics the surface stress is assumed to be proportional to the vertically averaged wind momentum [Eq. (3)] for separation of mechanisms. It may be interesting to examine vertically averaged equations without this assumption. Equations (5) and (6) are then reduced to

$$V_x - U_y = \frac{1}{f} \nabla^2 P - \frac{1}{f} \frac{\mathbf{V} \cdot \boldsymbol{\tau}(Z)}{Z} - \frac{1}{f} \mathbf{V} \cdot \mathbf{A} + \frac{1}{f} \frac{\mathbf{V} \cdot \boldsymbol{\tau}(0)}{Z} \quad \text{and} \quad (8)$$

$$-U_x - V_y = -\frac{1}{f} \frac{\mathbf{V} \times \boldsymbol{\tau}(Z)}{Z} - \frac{1}{f} \mathbf{V} \times \mathbf{A} + \frac{1}{f} \frac{\mathbf{V} \times \boldsymbol{\tau}(0)}{Z}, \quad (9)$$

respectively. There can be two approaches for which terms are used as the target to be explained. In one approach, target terms are the terms in the left-hand side, the same as in our diagnostics described in section 2a. In the other approach, target terms are the surface stress terms [the last terms in Eqs. (8) and (9)]. One apparent shortcoming common in these approaches is that one cannot evaluate the contribution of the PA mechanism using Eq. (9), as there is no explicit pressure term there, though the PA mechanism cannot be ignored for both the wind convergence and curl as shown above (Table 1). We will explain the results of these two approaches in this subsection.

The first approach [i.e., target terms are on the left-hand side of Eqs. (8) and (9)] gives a quite different impression

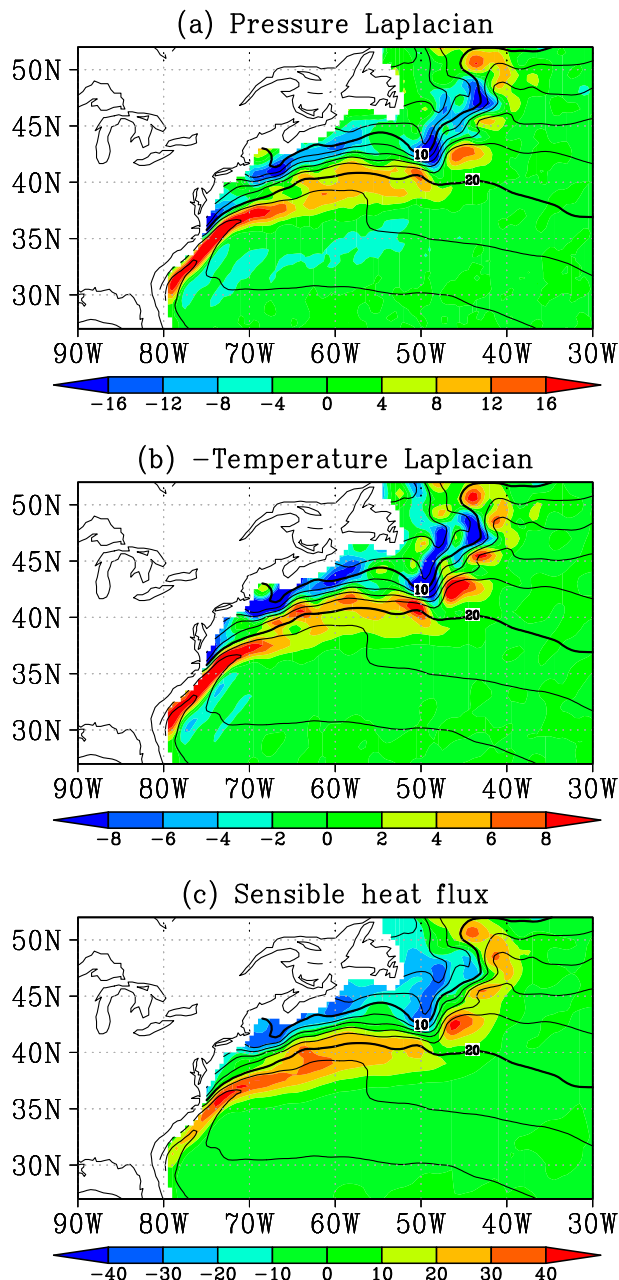


FIG. 7. Annual-mean climatology of (a) vertically averaged pressure Laplacian ( $10^{-10} \text{ Pa m}^{-2}$ ), (b) sign-reversed vertically averaged temperature Laplacian ( $10^{-11} \text{ K m}^{-2}$ ), and (c) sensible heat flux from ocean to atmosphere ( $\text{W m}^{-2}$ ).

from what was explained in the previous subsection. Each term of Eq. (8) for the momentum curl is shown in Fig. 9. The terms for pressure and downward momentum inputs without the assumption (Fig. 9) are about twofold larger than those with the assumption (Fig. 6). Without the assumption, the pressure term appears to be larger (Fig. 9a) than the downward momentum input term (Fig. 9b), in contrast to the diagnostics with the assumption described

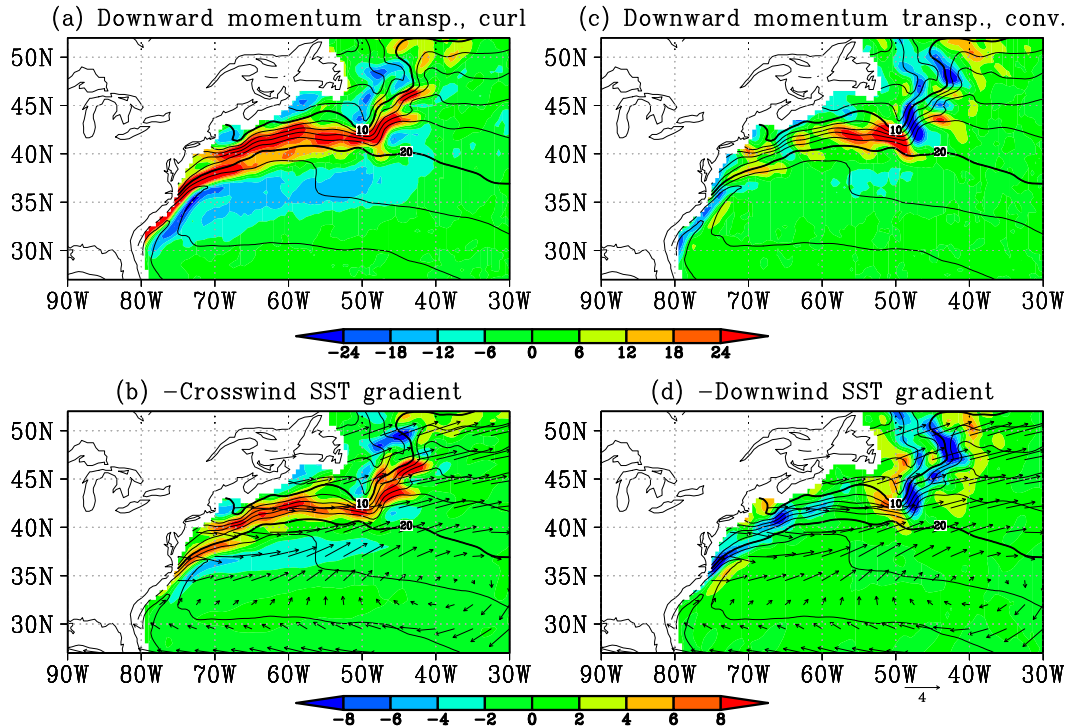


FIG. 8. Annual-mean climatology of (a) curl of downward momentum transport from the top of the surface layer (color,  $10^{-10} \text{ kg m}^{-3} \text{ s}^{-2}$ ), (b) sign-reversed crosswind SST gradient (color,  $10^{-6} \text{ K s}^{-1}$ ), (c) convergence of downward momentum transport (color,  $10^{-10} \text{ kg m}^{-3} \text{ s}^{-2}$ ), and (d) sign-reversed downwind SST gradient (color,  $10^{-6} \text{ K s}^{-1}$ ). Vectors show unfiltered 10-m wind ( $\text{m s}^{-1}$ ) with its reference vector in (d).

above. The apparent discrepancy, of course, arises from the treatment of the surface stress. In this approach, the surface stress is treated as a forcing, but it is internally determined to be associated with the respective mechanisms. The present results demonstrate that an analysis in which surface stress is treated as a forcing could lead to an erroneous interpretation.

The second approach [target variables are surface stress terms in Eqs. (8) and (9)] may be better than the first approach. In this case, Eq. (8) [Eq. (9)] is used to understand the mechanism of the surface wind stress convergence/divergence (curl). Figure 9 shows this approach works to some extent. The target surface stress convergence (sign reversed; Fig. 9d) is mostly explained by the pressure term (Fig. 9a), consistent with the dominant role of the PA mechanism for the wind momentum convergence in our diagnostics (Table 1). A difficulty of this approach is that the left-hand sides of these equations cannot be related to respective mechanisms, leaving uncertainty in determining the contributions of the respective mechanisms. Indeed, the standard deviations of the left-hand sides of Eqs. (8) and (9) are 34% and 43% of those of target terms, respectively. Regression analysis similar to Table 1 indicates the primary terms are consistent with the diagnostics shown

above, but the relative contribution of the primary and secondary terms are quite different. Furthermore, as mentioned above, the contribution of the PA mechanism for the wind stress curl cannot be estimated based on Eq. (9), resulting in the PA mechanism contribution being minor, even compared with the horizontal advection by design, but our diagnostics suggest that the contribution of the PA mechanism to the wind momentum curl is about one-third of that of the DMM mechanism (Table 1). Consequently, this approach is useful to find the largest contribution among the pressure, downward momentum mixing, and horizontal advection terms at least annual-mean fields over the Gulf Stream, but quantitative estimation of the contributions of respective terms is difficult.

#### 4. Diagnostics of seasonal variation

The diagnostics for surface-layer momentum curl and convergence can be applied to monthly climatology data. Though the latitude of the westerly jet changes with the season, the spatial pattern of surface-layer curl or convergence in each season (not shown) is actually similar to the pattern for annual-mean data (Fig. 4), indicating that this can be recognized as the atmospheric response to the ocean. The pattern resulting from the pressure or

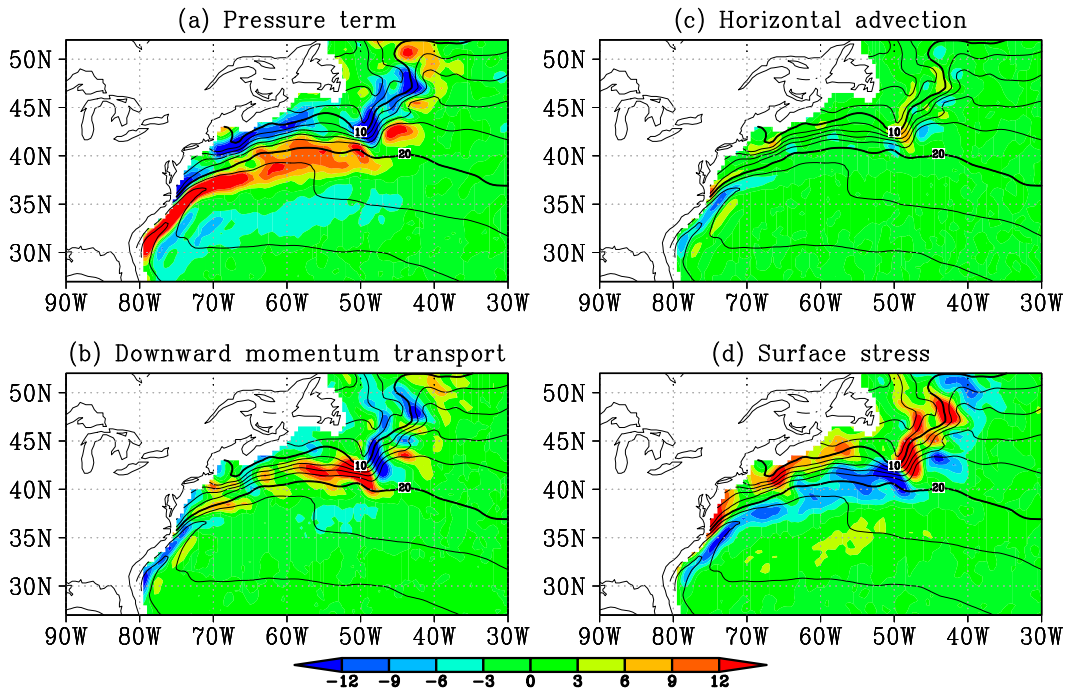


FIG. 9. Annual-mean climatology of the separate terms of the momentum curl in Eq. (8) (color,  $10^{-6} \text{ kg s}^{-1}$ ). Shown are the terms for (a) pressure, (b) downward momentum transport, (c) horizontal advection, and (d) surface stress. Note that the color scale is different from the one shown in Fig. 6.

downward momentum input terms is also similar, but its magnitude does vary from month to month. Hence, to examine the seasonal variation of the atmospheric response to the Gulf Stream, we simply evaluate the spatial variance of the pattern. Figure 10 shows the root-mean-squares (RMSs) of simulated momentum curl and convergence based on monthly-mean climatology. The convergence is strong in winter and weak during the rest of the year, whereas the magnitude of curl is roughly the same throughout the year.

In all seasons, the terms for the PA and DMM mechanisms are dominant, and the other terms can be ignored. Hence, the seasonal variation of momentum curl and convergence is attributed to seasonal variation of the PA or DMM mechanism. Recalling the terms in the diagnostic equations [Eqs. (5) and (6)], we have three possible explanations for the seasonal variation: the Laplacian of surface-layer pressure, the spatial derivative of downward momentum inputs, and the frictional parameter  $\varepsilon$ . It should be emphasized that we may think of  $\nabla^2 P$  as the PA mechanism and  $\nabla \times \tau(Z)$  as the DMM mechanism for momentum curl and  $\nabla^2 P$  as the PA mechanism and  $\nabla \cdot \tau(Z)$  as the DMM mechanism for momentum convergence, but the coefficients of  $[\varepsilon/(\varepsilon^2 + f^2), f/(\varepsilon^2 + f^2)]$  control the magnitude. Both the Laplacian of pressure and the spatial derivative of downward momentum inputs (Fig. 11) show clear

seasonal variations, with values in winter almost twofold larger than values in summer. In contrast, coefficients  $[\varepsilon/(\varepsilon^2 + f^2), f/(\varepsilon^2 + f^2)]$  have seasonal variation with large values in summer (Fig. 12b), owing to the frictional parameter  $\varepsilon$  being large in winter and small in summer (Fig. 12a). This is probably because the large heat flux to the atmosphere tends to cause unstable conditions in winter. Therefore, the Laplacian of

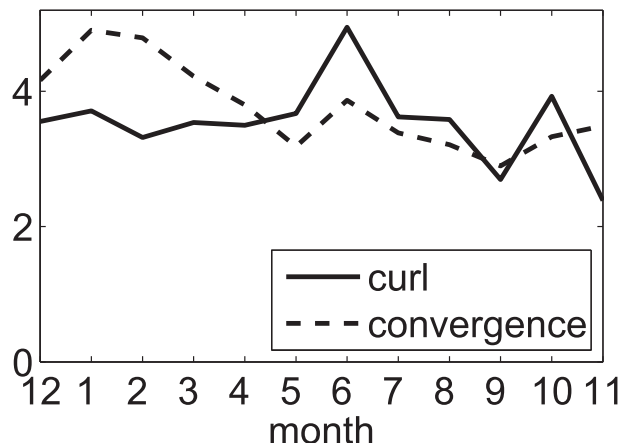


FIG. 10. Seasonal variation in RMS of the spatial variance of the momentum curl (solid line) and RMS of the momentum convergence (dashed line) in the parallelogram area shown in Fig. 1 ( $10^{-6} \text{ kg s}^{-1}$ ).

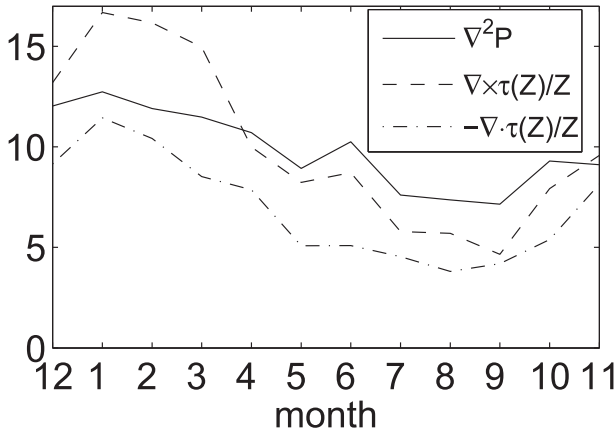


FIG. 11. Seasonal variation in RMS of the spatial variance of the Laplacian of surface-layer pressure (solid line), RMS of curl of downward momentum inputs (dashed line), and RMS of convergence of downward momentum inputs (dashed-dotted line) ( $10^{-10} \text{ kg m}^{-3} \text{ s}^{-2}$ ).

surface-layer pressure and the spatial derivative of downward momentum inputs are out of phase with the coefficients involving the frictional parameter. For the momentum curl, this counteraction is roughly balanced, and thus no prominent seasonal variation is seen in Fig. 10. For the momentum convergence, in which the PA mechanism is dominant throughout the year (not shown), the weak seasonal variation of the coefficient  $\varepsilon/(\varepsilon^2 + f^2)$  is not enough to cancel out the seasonal variation in the Laplacian of surface-layer pressure  $\nabla^2 P$ , and thus the seasonal variation of the convergence is in phase with the seasonal variation of the pressure Laplacian. These results indicate that, in regard to the seasonal variation, the frictional parameter plays an important role in the near-surface wind response to SSTs.

## 5. Discussion and conclusions

We have explored the mechanisms of near-surface winds by using regional atmospheric model outputs and explained the spatial structures of vertically averaged momentum curl and convergence. Extending Takatama et al. (2012), we constructed full diagnostics for the surface-layer momentum vector, its curl, and its convergence and clarified the effect of the pressure anomalies and downward momentum transport in the surface-layer system to evaluate the contribution of the PA and DMM mechanisms to the near-surface wind response to SST fronts. Furthermore, the diagnostics can be used for analyzing the wind stress instead of the wind momentum by multiplying  $\varepsilon Z$  by both sides of Eqs. (4)–(6). The key points of our diagnostics are 1) to separate the stress term

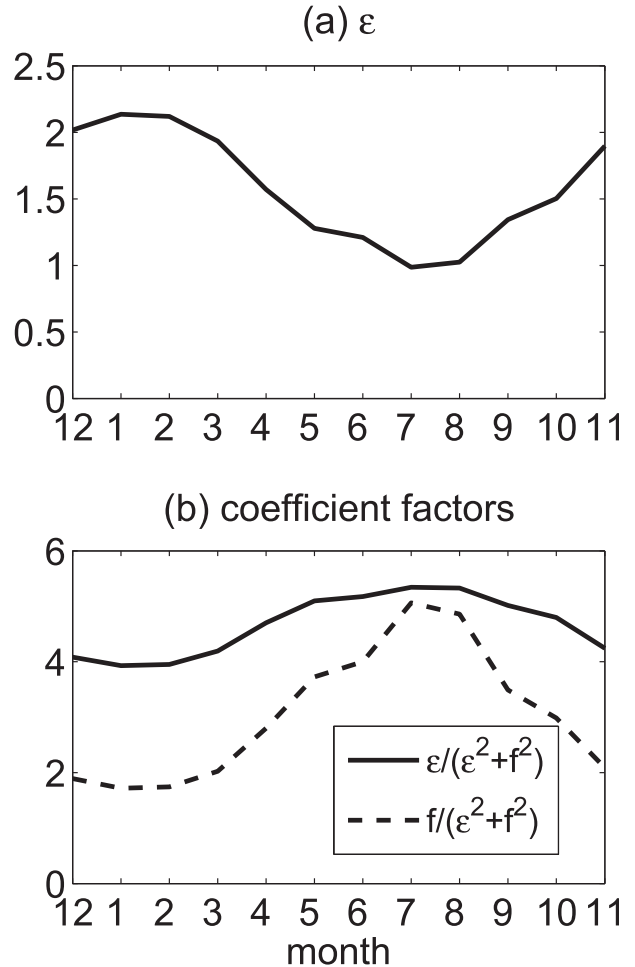


FIG. 12. Seasonal variation in (a) the frictional parameter  $\varepsilon$  ( $10^{-4} \text{ s}^{-1}$ ) and (b) coefficients of  $\varepsilon/(\varepsilon^2 + f^2)$  (solid line) and  $f/(\varepsilon^2 + f^2)$  (dashed line) ( $10^3 \text{ s}$ ). Both are averaged over the parallelogram area shown in Fig. 1.

in the momentum equation into downward momentum transport from the top of the surface layer and the surface wind stress by vertically integrating over the surface layer [Eq. (2)] and 2) to assume that the surface wind stress is linearly proportional to the vertically averaged momentum [Eq. (3)]. Though the PA and DMM mechanisms work simultaneously in the midlatitude MABL, the present diagnostic method successfully evaluated the effects of the separate mechanisms on surface-layer momentum curl [Eq. (5)] and convergence [Eq. (6)].

We have applied the diagnostics to a 5-yr simulation of iRAM focusing on the near-surface response to the Gulf Stream. Analysis of the annual-mean data revealed that the near-surface wind curl over the Gulf Stream is governed by the DMM mechanism, and the convergence is mainly due to the PA mechanism (Fig. 6; Table 1). Their

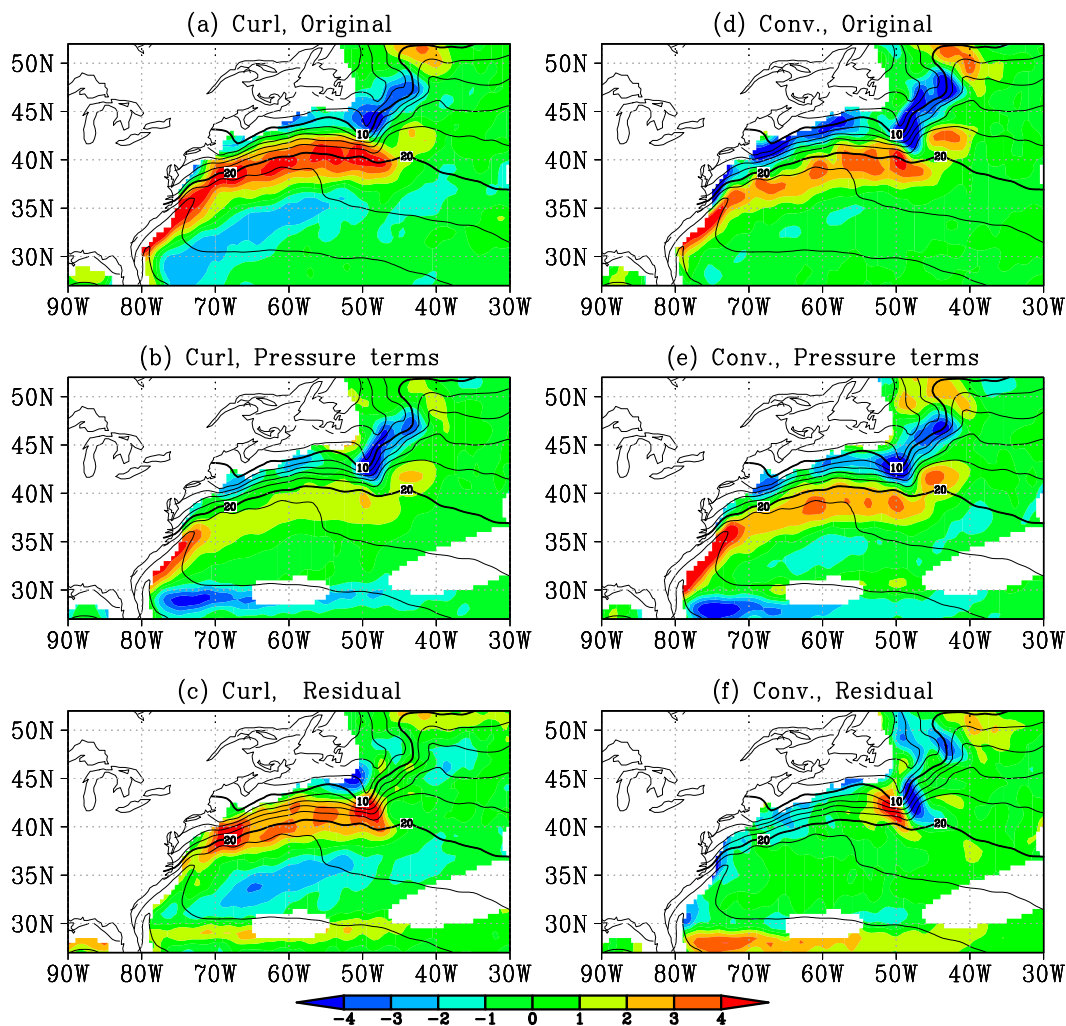


FIG. 13. Annual-mean climatology of (a)–(c) horizontal momentum curl and (d)–(f) convergence around the Gulf Stream obtained from the CFSR (color,  $10^{-6} \text{ kg s}^{-1}$ ). (a),(d) Original vertically averaged momentum; (b),(e) diagnosed curl resulting from the pressure terms; and (c),(f) residual terms. Note that the color scale is different from the one shown in Fig. 6.

relative contributions depend on the background wind direction with respect to SST fronts. The DMM mechanism contributes more to wind curl than to wind convergence in the Gulf Stream region west of  $55^{\circ}\text{W}$ , where the background wind blows parallel to the SST front (Fig. 8). In contrast, the PA mechanism is basically independent of the background wind direction, because the pressure Laplacian simply corresponds to the heat flux distribution (Fig. 7). Since the difference in magnitude between the convergence and curl due to the PA mechanism is determined by the ratio of the frictional parameter to the Coriolis parameter [Eqs. (5) and (6)], this mechanism contributes more strongly to convergence than to curl in this region. The above result is similar to the result based on the monthly climatology, but the momentum convergence response (Fig. 10) has

moderate seasonal variation, which is induced by large seasonal variation in the Laplacian of surface-layer pressure (Fig. 11a) that exceeds the counteraction by the seasonal variation in  $\varepsilon/(\varepsilon^2 + f^2)$ . In contrast, the curl does not show prominent seasonal variation, because the seasonal variation in the downward momentum inputs is canceled out by the seasonal variation in the coefficient of  $f/(\varepsilon^2 + f^2)$  (Fig. 10). It is interesting to note that O'Neill et al. (2010) found a nonnegligible contribution from horizontal advection in the Southern Ocean, but horizontal advection can be ignored in the present study. A possible explanation for this discrepancy is a difference of spatial scale. While they analyzed eddy scale SST anomaly fields obtained from 1-month simulations, we analyzed 5-yr-averaged frontal-scale fields. Nevertheless, the contribution of the horizontal

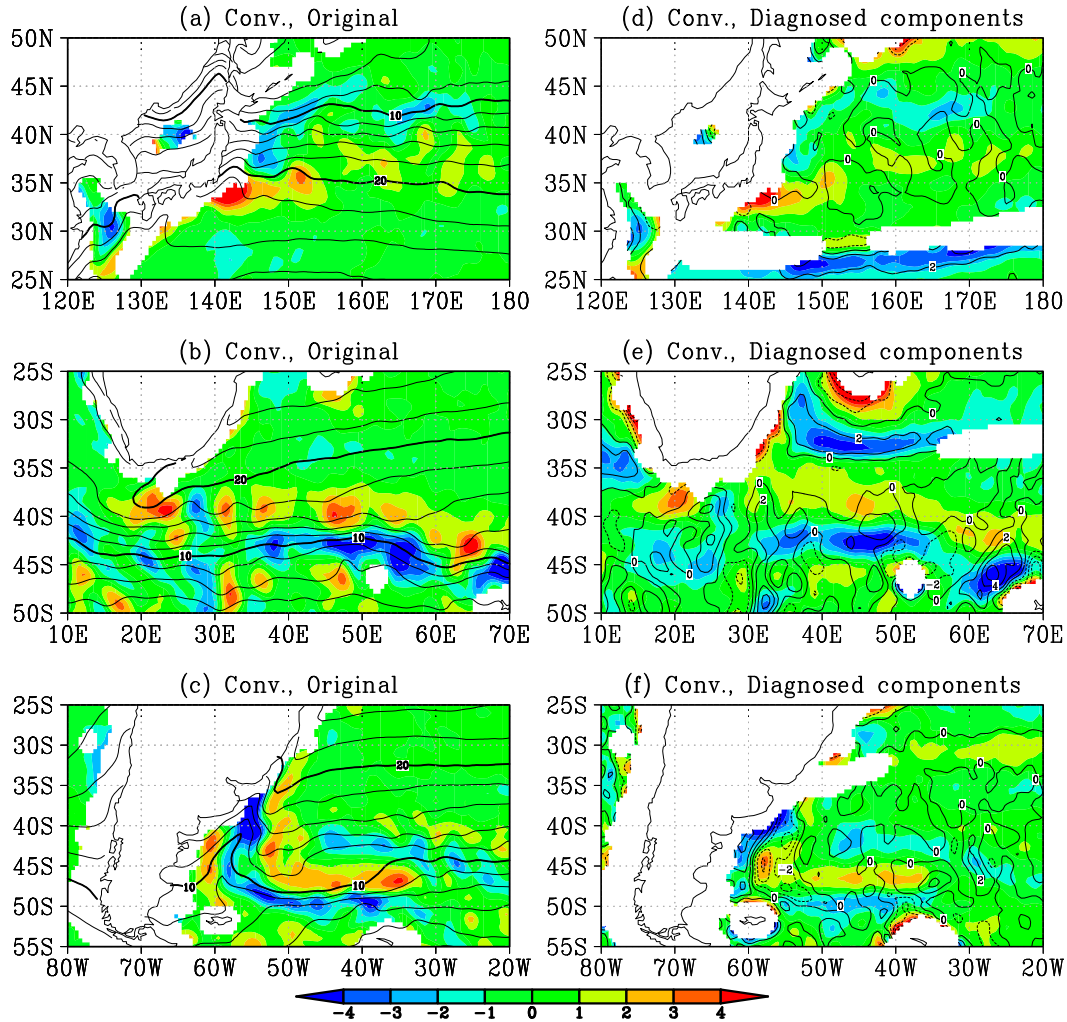


FIG. 14. (a)–(c) Annual-mean climatology of original momentum convergence (color,  $10^{-6} \text{ kg s}^{-1}$ ) obtained from the CFSR, and (d)–(f) diagnosed convergence resulting from the pressure terms (color,  $10^{-6} \text{ kg s}^{-1}$ ) and the residual terms (contour,  $2 \times 10^{-6} \text{ kg s}^{-1}$  interval) for three western boundary current regions: (a),(d) the Kuroshio Extension; (b),(e) the Agulhas Return Current; and (c),(f) the Brazil–Malvinas confluence.

advection remains small even in our high-resolution experiment, and we can therefore argue that the contribution is not large over the Gulf Stream region.

It is maybe interesting to apply some of our diagnostics to other atmospheric model outputs or reanalysis datasets. In particular, the pressure terms can be calculated by using the SLPs and geopotential heights in standard meteorological outputs. Therefore, the contribution of the pressure terms in a wide range of atmospheric numerical models and reanalysis datasets can be estimated by using our diagnostics. According to the diagnostics, the subtraction of the pressure terms from the total is, in practice, a good approximation for the downward momentum input terms. We here attempt this approach, using the NCEP Climate Forecast System Reanalysis (CFSR; Saha et al. 2010), which provides high-resolution ( $0.5^\circ \times 0.5^\circ$ )

reanalysis data. Although the CFSR also provides turbulent mixing terms, which could be used to evaluate downward momentum inputs from aloft, we will report the use of these terms in our full diagnostics in a future study. This is because, before using mixing terms in the CFSR to our diagnostics, one needs to carefully examine the validity of closeness of the momentum budget, which can be biased in an assimilation product, and the impacts of coarse resolution for mixing terms, which are provided on a  $1.0^\circ \times 1.0^\circ$  grid in contrast to a finer  $0.5^\circ \times 0.5^\circ$  grid for pressure, velocity, and surface stress terms.

Figure 13 shows the diagnostic for momentum curl and convergence in the surface layer around the Gulf Stream in the analysis, where the annual mean is taken as the 5-yr average for the same period as our numerical integration. The major features of the momentum curl and convergence

in the CFSR are consistent with our simulations. The pressure terms govern the momentum convergence and make a small contribution to curl. The spatial patterns of residual components are similar to those resulting from the downward momentum in our diagnostics shown in Fig. 6 for both the convergence and curl. The spatial patterns based on the CFSR are generally broader, perhaps because the SST gradients of the Gulf Stream front are slightly weaker in this dataset than in RTGSST.

The overall agreement between the full diagnosis using model output and the indirect estimation using the CFSR encourages us to apply our approach to other regions. Figure 14 shows the momentum convergence and its components resulting from the pressure terms and the residual terms over the other major western boundary currents obtained from the CFSR: the Kuroshio Extension, the Agulhas Return Current, and the Brazil–Malvinas confluence. Over the Kuroshio Extension (Figs. 14a,d), the Agulhas Return Current (Figs. 14b,e), and the offshore region of the Brazil–Malvinas confluence (east of 55°W, especially along 48°S; Figs. 14c,f), the pressure terms explain the momentum convergence well, similar to the results over the upstream region of the Gulf Stream. On the other hand, the residual terms yield strong convergence over the nearshore region (west of 55°W) of the Brazil–Malvinas confluence (Figs. 14c,f), reminiscent of the downstream region of the Gulf Stream. In the case of the former regions where the background wind blows parallel to the SST front, the PA mechanism dominantly contributes to momentum convergence. In the latter regions, the DMM mechanism is dominant instead. This is attributed to the DMM mechanism tending to be strongly influenced by the direction of background wind and SST fronts. These results suggest that the orientation of SST fronts with respect to the background wind direction is an important parameter when considering the dominant mechanism working in the surface-layer system over the western boundary currents.

*Acknowledgments.* We thank the three anonymous reviewers for providing useful comments and suggestions. This research was supported by the Japan Agency for Marine–Earth Science and Technology (JAMSTEC), by the National Aeronautics and Space Administration (NASA) through Grant NNX07AG53G, and by National Oceanic and Atmospheric Administration (NOAA) through Grant NA11NMF4320128, which funds research at the International Pacific Research Center. We gratefully acknowledge support from the Office of Science, U.S. Department of Energy Grants DE-SC0006766 and DE-SC0005111 and from the National Science Foundation through Grant NSF OCE05-50233. This research was also supported by a Grant-in-Aid for

Scientific Research on Innovative Areas (22106008), a Grant-in-Aid for Scientific Research (A) (22244057), and the Research Program on Climate Change Adaptation, all of which are funded by the Ministry of Education, Culture, Sports, Science and Technology of Japan.

## REFERENCES

- Brachet, S., F. Codron, Y. Feliks, M. Ghil, H. Le Treut, and E. Simonnet, 2012: Atmospheric circulations induced by a midlatitude SST front: A GCM study. *J. Climate*, **25**, 1847–1853, doi:10.1175/JCLI-D-11-00329.1.
- Bryan, F. O., R. Tomas, J. M. Dennis, D. B. Chelton, N. G. Loeb, and J. L. McClean, 2010: Frontal scale air–sea interaction in high-resolution coupled climate models. *J. Climate*, **23**, 6277–6291, doi:10.1175/2010JCLI3665.1.
- Businger, J. A., and W. J. Shaw, 1984: The response of the marine boundary layer to mesoscale variations in sea-surface temperature. *Dyn. Atmos. Oceans*, **8**, 267–281, doi:10.1016/0377-0265(84)90012-5.
- Chelton, D. B., and S.-P. Xie, 2010: Coupled ocean–atmosphere interaction at oceanic mesoscales. *Oceanography*, **23**, 52–69, doi:10.5670/oceanog.2010.05.
- , and Coauthors, 2001: Observations of coupling between surface wind stress and sea surface temperature in the eastern tropical Pacific. *J. Climate*, **14**, 1479–1498, doi:10.1175/1520-0442(2001)014<1479:OOCBSW>2.0.CO;2.
- , M. G. Schlax, M. H. Freilich, and R. F. Milliff, 2004: Satellite measurements reveal persistent small-scale features in ocean winds. *Science*, **303**, 978–983, doi:10.1126/science.1091901.
- , —, and R. M. Samelson, 2007: Summertime coupling between sea surface temperature and wind stress in the California Current System. *J. Phys. Oceanogr.*, **37**, 495–517, doi:10.1175/JPO3025.1.
- Deardorff, J. W., 1968: Dependence of air–sea transfer coefficients on bulk stability. *J. Geophys. Res.*, **73**, 2549–2557, doi:10.1029/JB073i008p02549.
- Gemmill, W., B. Katz, and X. Li, 2007: Daily real-time, global sea surface temperature—High-resolution analysis: RTG\_SST\_HR. NCEP/EMC Tech. Rep. 260, 39 pp. [Available online at <http://polar.ncep.noaa.gov/mmab/papers/tm260/MMAB260.pdf>.]
- Hand, R., N. S. Keenlyside, N.-E. Omrani, and M. Latif, 2014: Simulated response to inter-annual SST variations in the Gulf Stream region. *Climate Dyn.*, **42**, 715–731, doi:10.1007/s00382-013-1715-y.
- Hayes, S. P., M. J. McPhaden, and J. M. Wallace, 1989: The influence of sea-surface temperature on surface wind in the eastern equatorial Pacific: Weekly to monthly variability. *J. Climate*, **2**, 1500–1506, doi:10.1175/1520-0442(1989)002<1500:TIOSST>2.0.CO;2.
- Iizuka, S., 2010: Simulations of wintertime precipitation in the vicinity of Japan: Sensitivity to fine-scale distributions of sea surface temperature. *J. Geophys. Res.*, **115**, D10107, doi:10.1029/2009JD012576.
- Kalnay, E., and Coauthors, 1996: The NCEP/NCAR 40-Year Reanalysis Project. *Bull. Amer. Meteor. Soc.*, **77**, 437–471, doi:10.1175/1520-0477(1996)077<0437:TNYRP>2.0.CO;2.
- Kuwano-Yoshida, A., S. Minobe, and S.-P. Xie, 2010: Precipitation response to the Gulf Stream in an atmospheric GCM. *J. Climate*, **23**, 3676–3698, doi:10.1175/2010JCLI3261.1.
- Lindzen, R. S., and S. Nigam, 1987: On the role of sea surface temperature gradients in forcing low-level winds and convergence

- in the tropics. *J. Atmos. Sci.*, **44**, 2418–2436, doi:10.1175/1520-0469(1987)044<2418:OTROSS>2.0.CO;2.
- Liu, W. T., 2002: Progress in scatterometer application. *J. Oceanogr.*, **58**, 121–136, doi:10.1023/A:1015832919110.
- , and X. Xie, 2008: Ocean–atmosphere momentum coupling in the Kuroshio Extension observed from space. *J. Oceanogr.*, **64**, 631–637, doi:10.1007/s10872-008-0053-x.
- , —, P. S. Polito, S.-P. Xie, and H. Hashizume, 2000: Atmospheric manifestation of tropical instability wave observed by QuikSCAT and tropical rain measuring mission. *Geophys. Res. Lett.*, **27**, 2545–2548, doi:10.1029/2000GL011545.
- , —, and P. P. Niiler, 2007: Ocean–atmosphere interaction over Agulhas Extension meanders. *J. Climate*, **20**, 5784–5797, doi:10.1175/2007JCLI1732.1.
- Maloney, E. D., and D. B. Chelton, 2006: An assessment of the sea surface temperature influence on surface wind stress in numerical weather prediction and climate models. *J. Climate*, **19**, 2743–2762, doi:10.1175/JCLI3728.1.
- Minobe, S., A. Kuwano-Yoshida, N. Komori, S.-P. Xie, and R. J. Small, 2008: Influence of the Gulf Stream on the troposphere. *Nature*, **452**, 206–209, doi:10.1038/nature06690.
- , M. Miyashita, A. Kuwano-Yoshida, H. Tokinaga, and S.-P. Xie, 2010: Atmospheric response to the Gulf Stream: Seasonal variations. *J. Climate*, **23**, 3699–3719, doi:10.1175/2010JCLI3359.1.
- Miyama, T., M. Nonaka, H. Nakamura, and A. Kuwano-Yoshida, 2012: A striking early-summer event of a convective rainband persistent along the warm Kuroshio in the East China Sea. *Tellus*, **64A**, 18962, doi:10.3402/tellusa.v64i0.18962.
- Nonaka, M., and S.-P. Xie, 2003: Covariations of sea surface temperature and wind over the Kuroshio and its extension: Evidence for ocean-to-atmosphere feedback. *J. Climate*, **16**, 1404–1413, doi:10.1175/1520-0442(2003)16<1404:COSSA>2.0.CO;2.
- O'Neill, L. W., 2012: Wind speed and stability effects on coupling between surface wind stress and SST observed from buoys and satellite. *J. Climate*, **25**, 1544–1569, doi:10.1175/JCLI-D-11-00121.1.
- , D. B. Chelton, and S. K. Esbensen, 2003: Observations of SST-induced perturbations of the wind stress field over the Southern Ocean on seasonal timescales. *J. Climate*, **16**, 2340–2354, doi:10.1175/2780.1.
- , —, —, and F. J. Wentz, 2005: High-resolution satellite measurements of the atmospheric boundary layer response to SST variations along the Agulhas Return Current. *J. Climate*, **18**, 2706–2723, doi:10.1175/JCLI3415.1.
- , S. K. Esbensen, N. Thum, R. M. Samelson, and D. B. Chelton, 2010: Dynamical analysis of the boundary layer and surface wind responses to mesoscale SST perturbations. *J. Climate*, **23**, 559–581, doi:10.1175/2009JCLI2662.1.
- Putrasahan, D. A., A. J. Miller, and H. Seo, 2013: Isolating mesoscale coupled ocean–atmosphere interactions in the Kuroshio Extension region. *Dyn. Atmos. Oceans*, **63**, 60–78, doi:10.1016/j.dynatmoce.2013.04.001.
- Reynolds, R. W., T. M. Smith, C. Liu, D. B. Chelton, K. S. Casey, and M. G. Schlax, 2007: Daily high-resolution-blended analyses for sea surface temperature. *J. Climate*, **20**, 5473–5496, doi:10.1175/2007JCLI1824.1.
- Saha, S., and Coauthors, 2010: The NCEP Climate Forecast System Reanalysis. *Bull. Amer. Meteor. Soc.*, **91**, 1015–1057, doi:10.1175/2010BAMS3001.1.
- Shimada, T., and S. Minobe, 2011: Global analysis of the pressure adjustment mechanism over sea surface temperature fronts using AIRS/Aqua data. *Geophys. Res. Lett.*, **38**, L06704, doi:10.1029/2010GL046625.
- Skyllingstad, E. D., D. Vickers, L. Mahrt, and R. M. Samelson, 2007: Effects of mesoscale sea-surface temperature fronts on the marine atmospheric boundary layer. *Bound.-Layer Meteor.*, **123**, 219–237, doi:10.1007/s10546-006-9127-8.
- Small, R. J., S.-P. Xie, and Y. Wang, 2003: Numerical simulation of atmospheric response to Pacific tropical instability waves. *J. Climate*, **16**, 3723–3741, doi:10.1175/1520-0442(2003)016<3723:NSOART>2.0.CO;2.
- , and Coauthors, 2008: Air–sea interaction over ocean fronts and eddies. *Dyn. Atmos. Oceans*, **45**, 274–319, doi:10.1016/j.dynatmoce.2008.01.001.
- Song, Q., P. Cornillon, and T. Hara, 2006: Surface wind response to oceanic fronts. *J. Geophys. Res.*, **111**, C12006, doi:10.1029/2006JC003680.
- Spall, M. A., 2007: Midlatitude wind stress–sea surface temperature coupling in the vicinity of ocean fronts. *J. Climate*, **20**, 3785–3801, doi:10.1175/JCLI4234.1.
- Sweet, W., R. Fett, J. Kerling, and P. La Violette, 1981: Air–sea interaction effects in the lower troposphere across the north wall of the Gulf Stream. *Mon. Wea. Rev.*, **109**, 1042–1052, doi:10.1175/1520-0493(1981)109<1042:ASIEIT>2.0.CO;2.
- Takatama, K., S. Minobe, M. Inatsu, and R. J. Small, 2012: Diagnostics for near-surface wind convergence/divergence response to the Gulf Stream in a regional atmospheric model. *Atmos. Sci. Lett.*, **13**, 16–21, doi:10.1002/asl.355.
- Tanimoto, Y., T. Kanenari, H. Tokinaga, and S.-P. Xie, 2011: Sea level pressure minimum along the Kuroshio and its extension. *J. Climate*, **24**, 4419–4434, doi:10.1175/2011JCLI4062.1.
- Tokinaga, H., Y. Tanimoto, and S.-P. Xie, 2005: SST-induced surface wind variations over the Brazil–Malvinas confluence: Satellite and in situ observations. *J. Climate*, **18**, 3470–3482, doi:10.1175/JCLI3485.1.
- , —, —, T. Sampe, H. Tomita, and H. Ichikawa, 2009: Ocean frontal effects on the vertical development of clouds over the western North Pacific: In situ and satellite observations. *J. Climate*, **22**, 4241–4260, doi:10.1175/2009JCLI2763.1.
- Wai, M. M.-K., and S. A. Stage, 1989: Dynamical analyses of marine atmospheric boundary layer structure near the Gulf Stream oceanic front. *Quart. J. Roy. Meteor. Soc.*, **115**, 29–44, doi:10.1002/qj.49711548503.
- Wallace, J. M., T. P. Mitchell, and C. Deser, 1989: The influence of sea surface temperature on surface wind in the eastern equatorial Pacific: Seasonal and interannual variability. *J. Climate*, **2**, 1492–1499, doi:10.1175/1520-0442(1989)002<1492:TIOSSA>2.0.CO;2.
- Wang, Y., O. L. Sen, and B. Wang, 2003: A highly resolved regional climate model (IPRC-RegCM) and its simulation of the 1998 severe precipitation event over China. Part I: Model description and verification of simulation. *J. Climate*, **16**, 1721–1738, doi:10.1175/1520-0442(2003)016<1721:AHRRCM>2.0.CO;2.
- Xie, S.-P., 2004: Satellite observations of cool ocean–atmosphere interaction. *Bull. Amer. Meteor. Soc.*, **85**, 195–208, doi:10.1175/BAMS-85-2-195.
- , J. Hafner, Y. Tanimoto, W. T. Liu, H. Tokinaga, and H. Xu, 2002: Bathymetric effect on the winter sea surface temperature and climate of the Yellow and East China Seas. *Geophys. Res. Lett.*, **29**, L2228, doi:10.1029/2002GL015884.